Absolute calibration of the Colour and Stereo Surface Imaging System (CaSSIS)

Nicolas Thomas [a,*], Antoine Pommerol [a], Miguel Almeida [a], Matthew Read [a], Gabriele Cremonese [b], Emanuele Simioni [b], Giovanni Munaretto [b,c], Thomas Weigel [d]

[a] Space Research and Planetology Division, Physikalisches Inst., Universität Bern, Switzerland
[b] INAF, Osservatorio Astronomico di Padova, Padova, Italy
[c] Department of Physics and Astronomy "G. Galilei", University of Padova, Padova, Italy
[d] Thales-Alenia Space Switzerland, Zurich, Switzerland

ARTICLE INFO

ABSTRACT

The Colour and Stereo Surface Imaging System (CaSSIS) onboard the ExoMars Trace Gas Orbiter (TGO) has observed several standard stars and Jupiter with the aim of deriving the absolute calibration factors that convert observed signal into reflectance ("I over F"). The targets were observed through all four colour filters and hence a relative calibration between the filters was possible. In addition, observations of Phobos acquired during the TGO capture orbits in 2016 were analysed in support of the relative colour calibration. The results show that CaSSIS was around 13% less sensitive than predicted (normalised to the RED filter) - a value that is larger than the formal uncertainty and therefore significant. The relative colour calibration shows CaSSIS to be 4% more sensitive in the BLU than modelled which is close to the relative uncertainty. The text describes the analysis approach and methods for the various targets and newly recommended conversion factors are provided in table form.

1. Introduction

The Colour and Stereo Surface Imaging System (CaSSIS) is the scientific imaging system on the European Space Agency/Roscosmos mission, ExoMars Trace Gas Orbiter (TGO). The spacecraft was launched from Baikonur on 14 March 2016 at 09:31 UT and entered orbit around Mars on 19 October 2016. The spacecraft then performed a series of aerobraking manoeuvres over the next 18 months to bring it into a roughly circular orbit (360 km × 420 km above the surface of Mars). The prime mission began on 21 April 2018.

Following the initial orbit insertion a short series of images were acquired of two spectrophotometric standard stars (π^2 Orionis and ξ^2 Cetae) from the European Southern Observatory (ESO) catalogue (https://www.eso.org/sci/observing/tools/standards.html) to provide absolute calibration of the CaSSIS instrument, i.e. factors for conversion from digital numbers (DN) per second to reflectance unit (usually referred to in the planetary community as "I over F" which we abbreviate here to I/F) (Danielson et al., 1981). Our first analyses of these standard stars (the Hamuy et al. standards, HR718 and HR1544; Hamuy et al. (1992) and Hamuy et al. (1994)) were inconsistent with predictions of these

conversion factors based on on-ground measurements of components. Following further observations of standard stars (HR5191 and HR4554) combined with previous observations of Jupiter and Phobos, we now have a consistent view of the absolute photometric performance of the instrument. This article presents the results of the analysis. In the next section, we shall provide a brief overview of the instrument focussing on the important points needed for this article. We shall then discuss the observations and the data reduction steps. In section 5, we present the results and discuss the remaining issues. We follow this with a short conclusion.

2. The CaSSIS instrument

CaSSIS has been described in full by Thomas et al. (2017). We repeat some details important for this paper here. The instrument comprises an off-axis reflective telescope with a focal length of 875 mm and a 13.5 cm diameter primary mirror (f/6.5). The field of view (FoV) is of 0.878° in the plane of symmetry and 1.336° in the cross-track direction. The 4 aspheric mirrors are made of ZERODUR®Expansion Class 0. All four mirrors carry a protected silver coating using a process previously

qualified for space applications by RUAG Space. The spectral response function of the telescope will be discussed below.

The detector is a derivative of the Raytheon Osprey 2k device that has also been used for the SIMBIOSYS instrument on BepiColombo (Cremonese et al., 2020). It is based on Hybrid Silicon PIN (Si PIN) complementary metal-oxide-semiconductor (CMOS) technology. The Si PIN diodes, being backside illuminated, have a 100% fill factor and very high quantum efficiency up to near-IR wavelengths, ranging from 4% at 400 nm up to a maximum of 91% at 800 nm at 293 K by taking advantage of the Raytheon anti-reflection coating. The detailed quantum efficiency (QE) of the detector and its temperature dependence will be discussed in the modelling section below. We note here, however, that the detector was held at 273 K in flight by using a heater. A radiator was mounted to the back of the detector which ensures that when TGO is above the dayside hemisphere, the detector temperature is below 273 K in all cases. A PT1000 sensor (accuracy $\approx$ 1 K) and an electrical heater are then used to stabilise the temperature. The temperature of the detector can rise above 273 K if TGO is above the nightside because, in this geometry, the Sun can strike the radiator. However, CaSSIS does not image Mars under these conditions. Hence, the detector temperature is well controlled and known.

The detector array is composed of 2048 x 2048 pixels with 10 $\mu m \times$ 10 μm pixel pitch. The CMOS process provides a full well capacity of about 90 000 electrons. The detector is read-out with 14 bit digital resolution. The combination of the pixel pitch and the focal length of the telescope leads to an angular scale of 11.36 $\mu rad/px$. The system was designed to operate in push-frame mode. The spacecraft was designed to be nadir-pointing in nominal condition flying over the surface at roughly 3 km/s. In push-frame mode, exposures are acquired rapidly in such a way that they cover the surface along track with sufficient overlap to allow reconstruction of a complete swath on ground during post-processing.

A composite interference filter was placed directly above the active surface of the detector. This was a significant modification to the SIM-BIOSYS detector assembly. In the case of CaSSIS, a set of four relatively broad filters, named PAN, RED, NIR, BLU, were deposited on a fused silica substrate. A dark mask was implemented between each filter. The design allowed imaging with the four filters simultaneously with a maximum exposure time matched to the ground-track velocity. Each filter exposure in a sequence would be typically 2048 px wide and either 280 or 256 px depending on the filter. A typical sequence would make 40 exposures with exposure times of around 1.5 ms in a single sequence at a repetition frequency of around 400 ms per exposure. From an altitude of 400 km, this leads to a swath of 9.3 km $\times$ 44.2 km (assuming 10% overlap) for the final image post-reconstruction. The choice of filters, the exposure repetition frequency, the width, and the exposure time are all programmable through the flight software and are commanded for each individual image through our planning software (Thomas et al., 2017).

Our nomenclature here should be noted. An exposure is one acquisition within a sequence of 30–60 exposures that can be reconstructed to produce a single image of the surface of Mars. Each sequence can be commanded to provide 1, 2, 3, or 4 windows from the detector corresponding to the four filters. Hence, a sequence can produce up to 4 colour images of the surface.

The central wavelengths of the filters were selected to match the filters in the HiRISE imaging system for NASA's Mars Reconnaissance Orbiter (McEwen et al., 2007). With the additional filter in the CaSSIS system, the response of the NIR filter in HiRISE was split into two filters (called here RED and NIR) in the CaSSIS system thereby providing additional information in the wavelength region between 800 and 1000 nm. The bandwidths were selected on the basis of a trade-off between signal to noise and colour differentiation. The spectral transmission curves will be discussed in a subsequent section. Preliminary effective bandwidths and wavelengths were given in Thomas et al. (2017).

The telescope of CaSSIS is mounted on a bearing that allows the instrument to rotate through a full 360°. In nominal nadir-pointing

spacecraft operation, the telescope is oriented so that it points 10° off-nadir. For a stereo imaging sequence, the telescope is rotated so that it is forward pointing and aligned with the ground-track. After acquisition of an image in this configuration, the telescope can be rotated by 180° to point in the backward direction and a second image is taken. This allows a stereo pair to be acquired within a 45 s period - the exact time depending upon the precise position of the spacecraft in its orbit about Mars and the elevation of the Martian topography being targeted. This feature has no influence on the photometry but was used to image Phobos twice within a few minutes as will be explained below. Further details on stereo acquisition are given in Thomas et al. (2017) while the procedure used to produce Digital Terrain models from the stereo images is described by Simioni et al. (2021).

CaSSIS was produced under significant time pressure with limited possibilities to perform an in-depth and careful calibration on ground prior to delivery to the spacecraft. The main functionality of the instrument was proven (including timing for the push frame system), the focus was checked and numerous bias and flat-field measurements made. The relative spectral response of the instrument within all four colour filters was also verified and shown to be consistent with our knowledge of the components. Many of these measurements are described in Roloff et al. (2017). Unfortunately, the absolute response of the instrument could not be characterized in the laboratory because of time pressure.

Following launch, observations have been carried out to determine the radiometric performance of the instrument including bias levels and flat-fields of the detector (using observations of Martian plains as a homogeneous source, for example). The analysis of these data and the results are given in Pommerol et al. submitted. The results will be used herein for the reduction of several sets of standard star images and observations of Jupiter and Phobos.

3. Observations

The dates and times of the acquisitions used to determine the absolute photometric performance are given in Table 1.

The stars were chosen in order to have high signal levels at exposure times comparable to those used for observing Mars ($\approx$1.5 ms). This necessitated using stars with visual (absolute) magnitudes less than about 3 resulting in a very limited number of potential targets with well-known spectrophotometric charactristics.

The images of the stars and Jupiter were obtained by staring at the targets and using spacecraft pointing to move the image of the target across the detector so that the image passed through each of the filters in turn. Effectively, the spacecraft was pointing the CaSSIS boresight at the target and then nodding to move the image across the detector. This was performed twice in all cases with different parts of the detector being used for the two spacecraft nodding sequences in order to identify and

Table 1
Dates and time ranges of observing sequences used.

Target	HR	Spectral type	V Magnitude	First acquisition date/UT time	Exposure times [ms]
π^2 Orionis	1544	A1V	4.36	2016-11-20 16.06.05	19.2, 48.0,96.0
ξ^2 Cetae	718	B9III	4.28	2016-11-24 15.51.05	19.2, 48.0, 96.0
Phobos	–			2016-11-26 23:13:24	3.84
Phobos	–			2016-11-26 23:24:16	3.84
Jupiter	–			2019-11-25 01.44.20	1.402, 2.899, 5.808
γ Ursae Majoris	4554	A0V	2.44	2021-01-04 12:19:35	4.704, 9.408, 15.880
η Ursae Majoris	5191	B3V	1.86	2021-01-05 11:53:35	2.506, 5.002, 13.200

eliminate local detector effects (e.g. inhomogeneities). The exposure times were pre-calculated according to the existing photometric model. Images were acquired with three exposure times in order to ensure an optimum choice for future analysis. During the analysis, it was found that for all four standard stars, the highest exposure time led to slight saturation of the detector in BLU and PAN. It was possible to identify these cases clearly and they were eliminated from further analysis.

For each exposure, 3 windows of 2048 px x 300 px were read-out of the array leading to a final image size of 2048 px x 900 px. While this was, of course, much larger than the size of the target image, it nonetheless allowed good determination of the background and was used extensively in the data reduction as will be described below.

At each position and for each exposure time, 9 exposures were acquired in a sequence. It has been observed that the detector exhibits a slightly higher background/bias level for the first images in such a sequence. The magnitude of this level decreases with the exposure number and is not visible after the 4th or 5th exposure. This artefact is related to the limited ability of the detector to reset the signal as already noted and investigated by Simioni et al. (2017) with the similar detector of SIMBIO-SYS. Images of the same detector area using the same imaging parameters but without the target being present were used to eliminate these effects. This occurred naturally when the star was moved to the next filter in the sequence. Because of the proximity of the target and the background on the sky, no changing sky background effects were expected. In essence, each exposure with the target was reduced using an exposure without the target acquired under identical conditions within an identical sequence at a position < 1° away from the stellar target. This straightforward sky image subtraction technique is optimum for this application.

Phobos was a special case. It was observed during the capture orbit phase after orbit insertion but before aerobraking had commenced. CaSSIS was aligned with the spacecraft motion relative to Phobos so that the image of the moon would pass through the field of view perpendicular to the long direction of the filters on the detector. Images were taken rapidly in the hope of catching the moon successfully within each filter. This was chosen as the method because the precise pointing of the instrument and the timing of the onboard commanding had not yet been completely established and (as will be seen) the image of Phobos was larger than the width of one filter element on the detector from that observing geometry. The observation was repeated by rotating CaSSIS by 180 deg and repeating the imaging sequence around 11 min later. The phase angle increased by just under 10° between the two observations. The geometries for the Phobos and Jupiter observations are shown in Table 3.

4. Data reduction

4.1. Stars

Throughout the data reduction, we have followed a principle that we

use exposures without the target but acquired under identical conditions to subtract any residual background from the target exposures. Strict adherence to this principle is critical for the reduction of the stellar data. Indeed, relatively long exposure times were often used for faint stars and we are aware that the bias and sensitivity of the detector depend on the exposure time, the imaging cadence and the position of the image in a sequence (Simioni et al., 2017; Roloff et al., 2017).

Both the exposure with the star and the corresponding exposure without star are first reduced by subtracting the bias and dividing by the flatfield (Pommerol et al., submitted). It should be noted that the flatfield is normalised such that the mean value over the detector is equal to one so that the mean of any residual bias is left unaltered by the division. The image without the star is then subtracted from the image with the star. It was already shown during the first commissioning campaign after launch that CaSSIS produces sharp images of stars with a roughly Gaussian Point Spread Function (PSF) and a narrow Full Width at Half Maximum (FWHM), smaller than 1.5 pixel (Gambicorti et al., 2017). Although the narrow PSF is key for providing sharp images of the Martian surface, it is not ideal for the photometry of point source targets where a PSF spread over a large number of pixels would be beneficial. It is also important to note that although the point spread function of the instrument can be approximated by a narrow 2D Gaussian shape, for photometric purposes, the PSF is broader in the wings (arising from contributions outside the first minimum of the Airy disc, spherical aberration, and scattering) and this needs to be taken into account. This is illustrated in Fig. 1 with an image of HR 4554. The top left panel shows the stellar image after bias correction and flat field. The top centre panel shows a background image corrected in the same way. Some residual background can be seen. The final stellar image after removing this residual is shown in the bottom left panel. The dynamic range of these images was strongly reduced to show details. The top right panel shows the same image as bottom left with less aggressive reduction in the dynamic range. A 2D Gaussian fit is often used to provide a convenient measure of the width of the PSF. The panel bottom centre shows a 2D Gaussian fit to the star and bottom right shows this Gaussian subtracted from the fully corrected image. Note that the image bottom right shows an array 2.5 times larger on the detector than the other images in the figure. This is to illustrate the remaining random noise in the image before extraction of the stellar signal. After subtraction of the 2D Gaussian, a residual around the subtracted core of the PSF can be seen out to a radius of around 8 pixels from the maximum.

We then use the classical stellar photometry algorithm DAOPHOT (Stetson, 1987) to obtain the total flux of the star using the "aperture photometry" technique. The total number of DN registered by the detector is obtained by the summation of the signal within a given radius around the centroid of the star. From the same image, a background level is estimated by summing signal values within an annulus defined around the star with given inner and outer radii. A residual background level is then subtracted from the star signal values taking into account the respective number of pixels in both areas. This operation is necessary even after the dark frame subtraction described before, as the overall bias of the detector is not constant for the first 5 framelets in any sequence and there is also slight variation in the bias signal from image to image (see Pommerol et al., submitted). The bias can only be predicted for Mars imaging (it cannot be extracted from the Mars data themselves) by performing dark observations of the nightside surface of the planet. We have studied 36 nightside images acquired at exposure times comparable to those used for dayside imaging (≈1.5 ms). The standard deviation of the mean bias in these images is 4.4 DN. The variation produces an error in the absolute photometry of the order of 0.05%–0.22% depending upon the filter used and the light level (assuming at least 2200 DN/px signal from the target). We have used several approaches to derive the flatfield which is normalised to one over the exposed areas of the detector. Based on the differences between the results of these calculations, we have computed a mean uncertainty over the detector of 0.072% in the flatfield at the pixel level.

In light of the results shown in Fig. 1 and after experimenting with

Table 2

Results of the stellar flux analysis for the four standard stars used in this study and the four colour filters of CaSSIS. Average fluxes in 10^3 DN/s followed by the relative standard deviation in %. The number of images used for each filter summed over all exposure times is given in parentheses afterwards.

Target star	BLU	PAN	RED	NIR
HR 718	441.1 (0.83%) (24)	407.6 (1.21%) (24)	107.0 (2.04%) (24)	92.0 (2.54%) (174)
HR 1544	401.9 (0.78%) (24)	398.5 (1.16%) (24)	110.4 (1.14%) (24)	95.8 (2.52%) (145)
HR 4554	2386.8 (1.18%) (86)	2287.2 (1.15%) (48)	622.2 (2.35%) (82)	550.4 (1.51%) (54)
HR 5191	4271.6 (1.32%) (85)	3534.3 (1.18%) (67)	880.8 (2.09%) (90)	695.3 (2.20%) (64)

Table 3

Signal generation rates compared to the model with the temperature of the detector assumed as 273 K for the QE values.

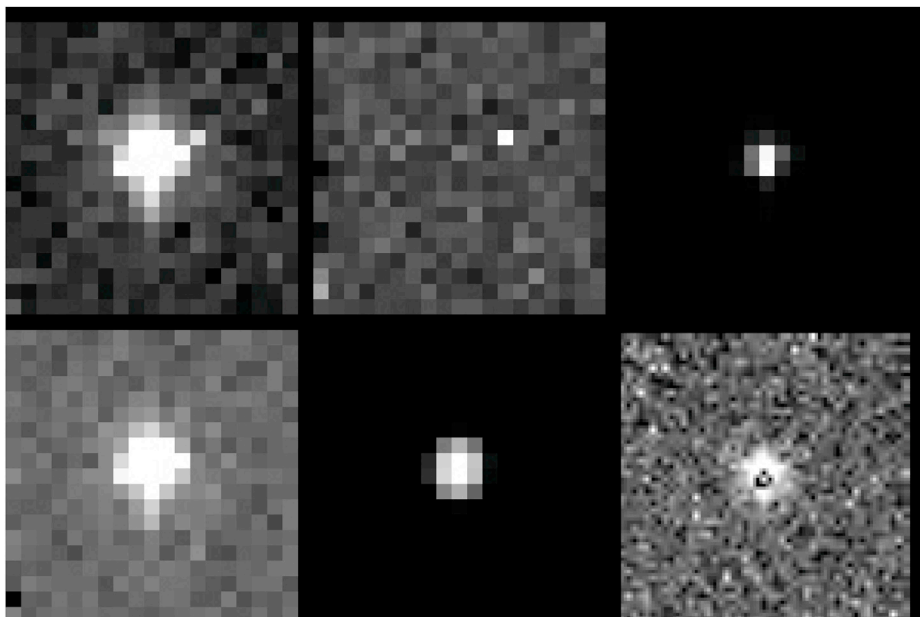| Target	r_h [AU]	Δ	Phase angle	Signal observed/predict [%]			
				BLU	PAN	RED	NIR
Phobos	1.387 1	7666 km	34.9	85.46	81.13	84.88	81.73
Phobos	1.387 1	7683 km	44.8	80.69	76.90	82.58	80.50
Jupiter	5.240 9	5.102 9 AU	18.02	86.34	82.48	84.93	80.84
HR 718	–	–	–	91.60	87.31	86.03	91.35
HR 1544	–	–	–	92.97	88.22	86.87	89.80
HR 4554	–	–	–	111.28	101.07	100.55	99.09
HR 5191	–	–	–	90.69	83.38	83.41	79.31

Fig. 1. Single image of star HR 4554 acquired through the BLU filter. Top left: Image after initial bias subtraction and flat-fielding. The image has been stretched non-linearly to show the structure of the point spread function far from the core. The ring indicates the ring for the aperture photometry computation. Top centre: An image acquired under identical conditions and with identical processing but with the star absent. Top right: The star image with removed residual and no non-linearly stretching. Bottom left: As Top right but with non-linear stretch again. Bottom centre: A 2D Gaussian fit to the signal. Bottom right: The stellar image after removal of the fitted 2D Gaussian. Note the extended coma which was not fit by the Gaussian fitting routine. The scale of the image bottom right is 2.5 times less than the other images to show more of the background.

different values, we choose a radius of 12 pixels around the centroid to collect the flux from the star and 20 and 40 px, respectively, for the internal and external radii of the background annulus. These values result from a compromise to capture as much as possible of the star signal while keeping the standard deviations for the resulting integrated DN values in each filter low. Using these values and according to our tests, we keep the standard deviations below or around 2.5% while capturing at least 99% of the stellar flux.

Integrated values of flux are calculated with this method for all individual exposures. The values are then sorted by exposure time and filter. All values extracted from the first exposure in a sequence are discarded as well as the overall minimum and maximum values found for each combination of filter and exposure time. Mean fluxes and standard deviations are finally calculated and the results are displayed in Figs. 2–5. Consequently, our standard acquisition sequence produces 24 stellar images to be averaged per colour. The commanded spacecraft motion means that these images are from 4 different positions on the detector. Plotted as a function of exposure time, all mean values of stellar flux obtained show an excellent linearity of the detector. The only exceptions are the flux values at the longest exposure time for BLU and PAN, which are slightly affected by saturation of the brightest pixel. The straight lines passing through non-saturated points pass close to the [0,0] origin, proving that the background removal is working well. A linear fit is performed on all values not affected by saturation (3 exposure times for RED and NIR, 2 for PAN and BLU) and the [0,0] origin point. The results of these fits are displayed as dashed lines on Figs. 2 to 5 and the values of the slopes and their 1-σ uncertainties are provided in Table 2.
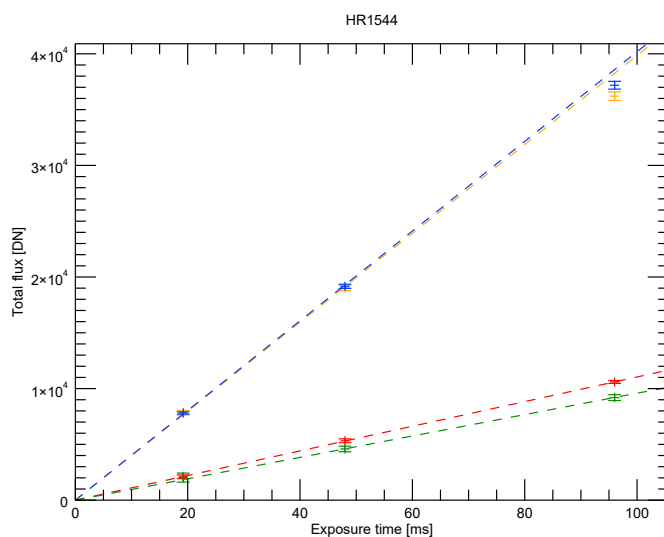

Fig. 2. Mean stellar fluxes and standard deviations for standard star HR1544 extracted for three different exposure times and the four colour filters of CaSSIS. Blue: BLU, Orange: PAN, Red: RED, Green: NIR, The dashed lines show the best linear fits of these data and the [0,0] origin point. The data for BLU and PAN at the longest exposure time are affected by saturation and excluded from the fitting procedure.
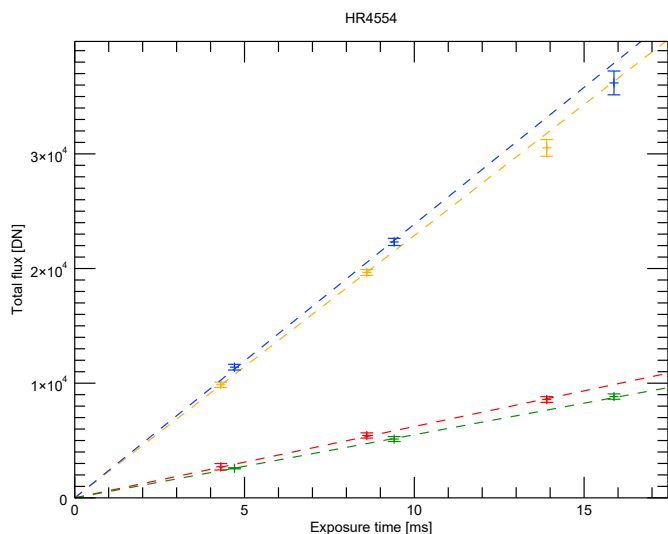
Fig. 3. Mean stellar fluxes and standard deviations for standard star HR4554 extracted for three different exposure times and the four colour filters of CaSSIS. Blue: BLU, Orange: PAN, Red: RED, Green: NIR, The dashed lines show the best linear fits performed on these data and the [0,0] origin point. The data for BLU and PAN at the longest exposure time are affected by saturation and excluded from the fitting procedure.
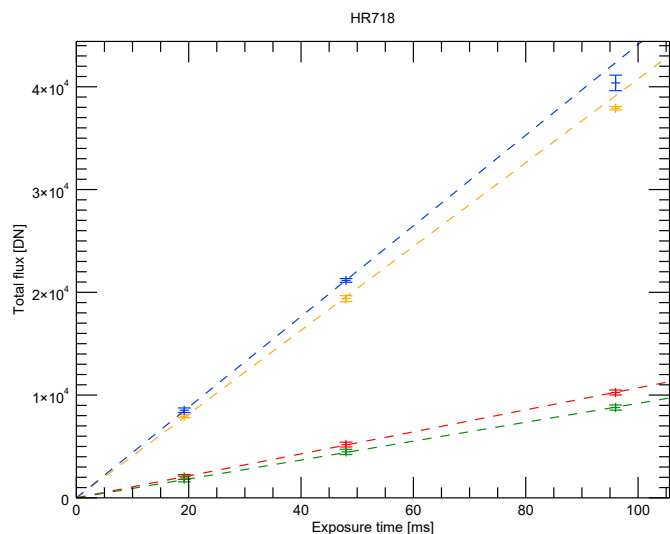

Fig. 5. Mean stellar fluxes and standard deviations for standard star HR718 extracted for three different exposure times and the four colour filters of CaSSIS. Blue: BLU, Orange: PAN, Red: RED, Green: NIR, The dashed lines show the best linear fits performed on these data and the [0,0] origin point. The data for BLU and PAN at the longest exposure time are affected by saturation and excluded from the fitting procedure.
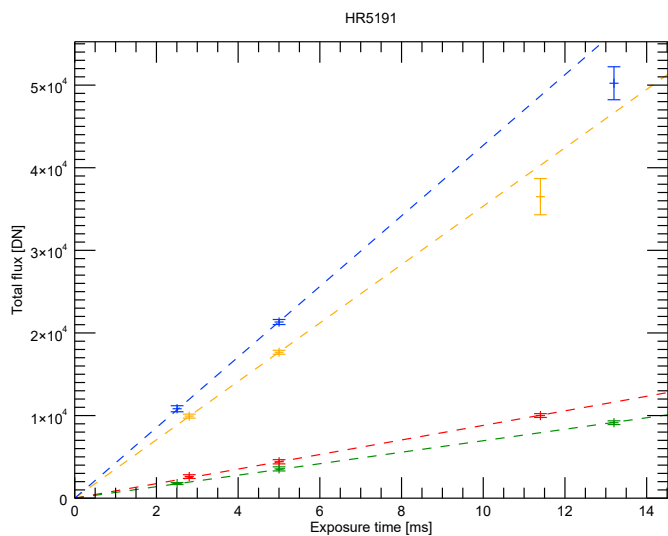
for by taking only the middle 7 values of the 9 image sequence for each exposure time.

The signals of all images acquired in an individual filter were then averaged with a weighting proportional to the exposure time to provide a single digital number generation rate for each filter in [DN/s]. A standard deviation was calculated based on the variation between the 7 individual exposures.

4.3. Phobos

The different approach to image acquisition required a slightly different approach to the reduction while maintaining the same basic principle of removing background images acquired under identical conditions as the image of the target.

The apparent size of Phobos was such that, in general, two adjacent exposures needed to be stitched together to produce a complete image of Phobos in one filter. Only then could the signal be integrated to produce a final digital number generation rate for the moon. However, the apparent motion of Phobos was fast - typically only 8 exposures in the sequence of 40 would contain signal from Phobos within any one filter. Consequently exposures from the same sequence could be used to provide the background for subtraction once the standard bias subtraction and flat field corrections had been performed. The first 3 exposures in the sequence were not used for background frames in order to avoid any issues connected to the slightly higher bias level observed in the first images of a sequence that was also noted above. A visualization of how the image passes through the field of view of the PAN filter using actual data is shown in Fig. 7.

We have reconstructed one complete image of Phobos in each filter in order to determine the digital number generation rate. Errors in the stitching of 1 pixel would correspond to an error in the final photometry in each filter of about $\pm 0.4\%$. For each filter, two images could be constructed - one acquired with CaSSIS looking forward towards the target and one from the sequence made 11 min later with CaSSIS looking back as TGO flew outward on its eccentric capture orbit. Because we have only two individual observations we have no real statistics and so we have to work through the calculations with no knowledge of the standard error. (Taking the square root of the signal underestimates the error by orders

Fig. 4. Mean stellar fluxes and standard deviations for standard star HR5191 extracted for three different exposure times and the four colour filters of CaSSIS. Blue: BLU, Orange: PAN, Red: RED, Green: NIR, The dashed lines show the best linear fits performed on these data and the [0,0] origin point. The data for BLU and PAN at the longest exposure time are affected by saturation and excluded from the fitting procedure.

4.2. Jupiter

The reduction of the Jupiter images followed that of the standard stars rather closely. Bias and flat fields were removed, both from images with Jupiter present, and from corresponding images acquired at identical positions within other sequences where Jupiter was absent. The background image was used to reduce residual background to below the 0.2% level. The signal was then summed over the visible disc of Jupiter taking into account the contribution from the extended PSF (Fig. 6). Possible outliers (resulting from, e.g. cosmic ray events) were accounted
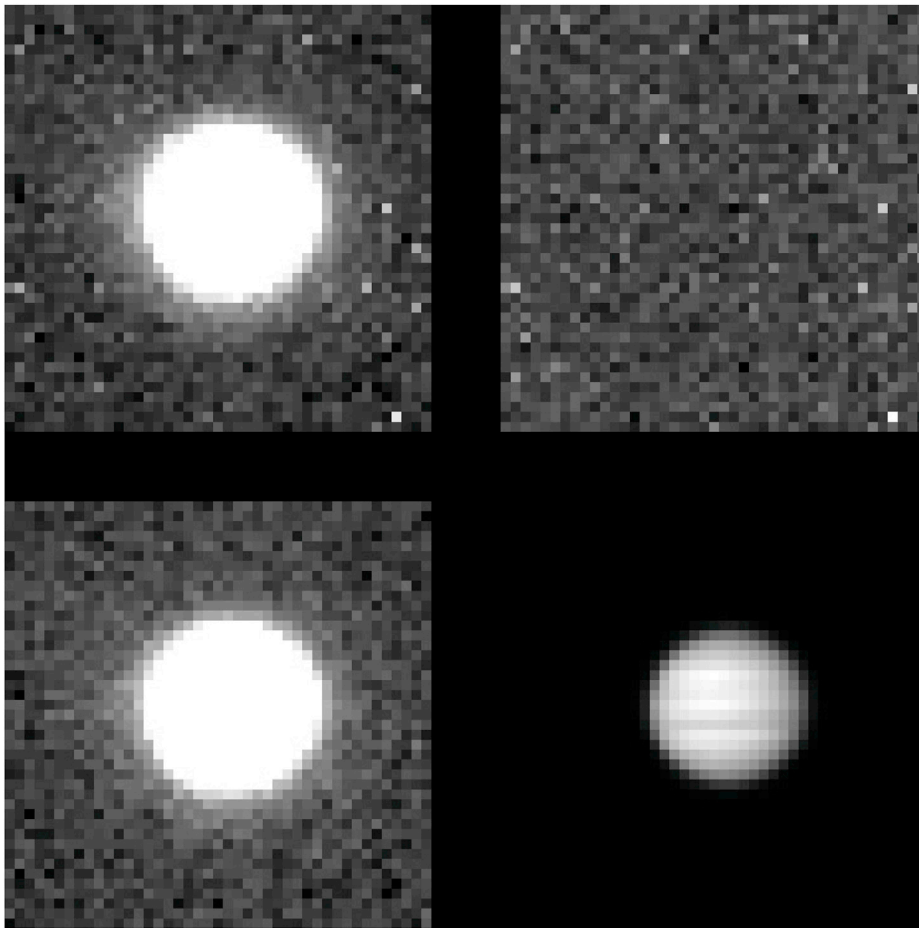
Fig. 6. Single image of Jupiter acquired through the BLU filter. Top left: Image after initial bias subtraction and flat-fielding. The image was clamped with a maximum of 200 DN to show the background. Top right: An image acquired under identical conditions and with identical processing but with Jupiter absent. Note the residual pattern evident in the top left frame. Bottom left: The corrected image of Jupiter clamped (maximum = 200 DN) to show the background. Bottom right: The image of Jupiter with no clamping. The banding in the atmosphere can be seen well.

Fig. 7. Five consecutive images in the PAN filter showing the apparent motion of Phobos over the detector. The images were acquired 1.5 s apart and have been subframed in the horizontal but not vertical direction. The image height was 252 pixels in this case with 1 pixel corresponding to around 88 m scale.

of magnitude.) The residual after the background subtraction provides a negligible influence on the final digital signal generation rate so that simple summation of the signal and division by the exposure time is adequate.

5. System model

5.1. Instrument properties

The entrance to the telescope is defined by an elliptical hole in a surface at the front of the telescope that is inclined to the incoming beam. This defines a circular beam with a 13.5 cm diameter that then proceeds to the primary mirror. The primary mirror is oversized compared to this entrance aperture size. The error on the size of entrance aperture is defined by the manufacturing errors and less than 1 mm in diameter. The reflectance of the telescope is given by its silver coating that has been measured by the manufacturer. There are four reflecting surfaces in the instrument. The combined reflectance for all four surfaces is shown in

Fig. 8 as the dashed line. The filter transmission functions have been measured by the manufacturer and are also shown in Fig. 8. The errors in these transmission and reflectance functions are not known but a value of 1–2% at near the peak transmission would not be unreasonable. Note the drop in telescope transmission close to the BLU filter low wavelength cut-off. Note also the small amount of transmission shortward of 400 nm in the BLU filter.

One of the key components of the instrument response is the quantum efficiency (QE) of the detector. The QE for the specific detector was measured at room temperature and is given by the thin solid line in Fig. 9. However, datasheets for the Osprey device indicate sensitivity to temperature in the blue and in the near-infrared. Using values given in the datasheet and interpolating linearly to 273 K (the detector temperature in the CaSSIS instrument), the QE curve appears different (Fig. 9). The near-IR shows a reduced sensitivity while the blue sensitivity is higher. The sensitivities at wavelengths corresponding to the RED and PAN are largely unaffected.

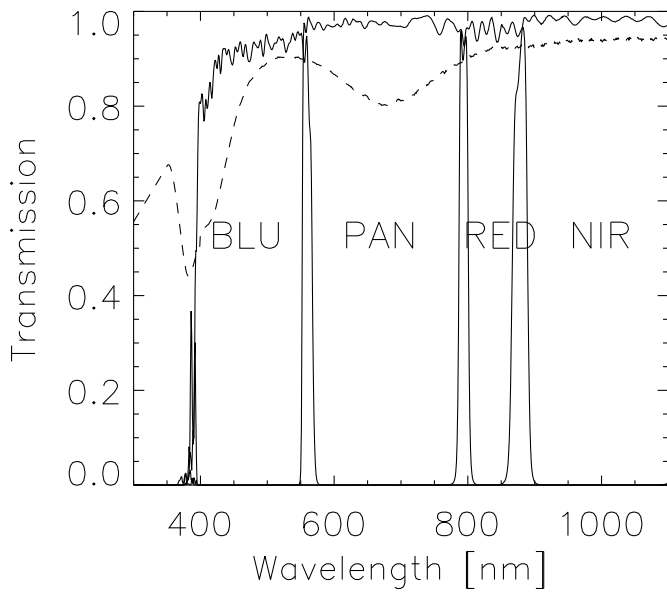The differences in the blue (highlighted in Fig. 9 by showing the ratio

Fig. 8. Solid lines: The filter transmission curves for the CaSSIS instrument. Dashed line: The telescope transmission curve computed from the reflectance of the silver coating used for the 4 mirrors.
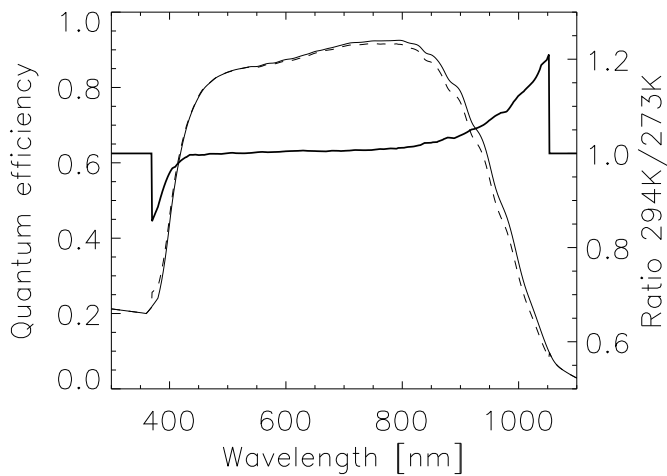

Fig. 9. Thin solid line: The nominal quantum efficiency curve of the detector for CaSSIS measured at room temperature. Dashed line: A linear extrapolation of the nominal QE curve to a temperature of 273 K assuming a similar behaviour of the detector to that shown in the Raytheon Osprey datasheet. Note the difference in the blue and near-IR regions of the spectrum. This is emphasized by the thick line which shows the ratio of the QE curve at 294 K to that at 273 K using the right-hand axis. There are 20% differences between the two curves close to the extremes in wavelength for which we have measurements.

between the QE at 294K to that at 273K) have relatively little effect because the filter cuts much of the signal below 385 nm. In the NIR, however, the 20% decrease in signal from 294K to 273K has a significant effect on the total signal observed by CaSSIS.

The value for detector gain (the conversion factor for electrons to digital number in units of e/DN) has been provided by the detector block supplier as 7.2 e/DN. We assume the decimal place indicates an error of around 1.5% on this number. However, the calculation of the system responsivity from the observations is not dependent upon this number.

5.2. Stars

The stellar fluxes used here have been taken from the European

Southern Observatory database (e.g. https://www.eso.org/sci/observing/tools/standards/spectra/hr4554.html for HR4554; retrieved 27 Jan. 2021).

The system responsivity to a stellar flux is then given by

$$R_s = \frac{1}{G} \int_0^\infty F(\lambda) \, M(\lambda) \, Q(\lambda) \, T(\lambda) \frac{\pi d^2}{4} \frac{\lambda}{hc} \, d\lambda \tag{1}$$

where d is the diameter of the aperture in [m^2], F is the input flux in [W m^{-2} nm^{-1}], M is the telescope transmission, T is the filter transmission, λ is the wavelength, Q is the quantum efficiency [electron/photon], and G is the detector gain in [electron DN^{-1}] (Thomas and Keller, 1990). The factor λ/hc is needed to convert the flux from an energy unit into a photon based unit. R_s is then in units of [DN s^{-1}] and can be compared directly with the observations. If the spectral response function is known then a deviation of the observed value of R_s from the predicted value would be indicative of an error in G or in the efficiency/transmission of one of the components.

5.3. Jupiter

The system responsivity to the flux from Jupiter, R_J uses a similar equation but F must be computed. For the solar flux at Jupiter, values at 1 nm intervals have been interpolated from Meftah et al. (2018). Note that there are significant differences (up to 3%) between these values and those given by Kurucz et al. (1984) in the near-IR. The wavelength-dependent flux from the target can then be computed using the equation

$$F(\lambda) = F_\odot(\lambda) \, p(\lambda) \, \varphi(\alpha, \lambda) \, \frac{r_J^2}{\Delta^2 \, r_h^2} \tag{2}$$

(Tomasko, 1976) where Δ is the observer-target distance, r_h is the heliocentric distance in [AU], $F_\odot$ is the solar flux at 1 AU, and r_J is the effective radius of Jupiter taking into account the object's oblateness and equal to 69 099 km p is the geometric albedo of Jupiter and φ is the phase function. The phase function is dependent upon the phase angle, α and has been shown to have some dependence on wavelength by Mayorga et al. (2016) using data from the CASSINI flyby in 2000.

The spectrum of Jupiter has been taken from Karkoschka (1998). It is to be noted that Karkoschka gives a full disc albedo at a phase angle of 6.8°. Hence this is not the geometric albedo, p. The work of Mayorga et al. (2016) has been used to correct for the phase angle difference between our observations and those of Karkoschka by using the CASSINI filters closest in central wavelength to the filters of CaSSIS. This allows us to compute $F(\lambda)$ and substitute into equation (1). We note that Gelino and Marley (2000) computed the photometric variability of an unresolved Jupiter at 410 nm and found it to be 0.04 magnitudes (corresponding to 3.7%) but there is limited knowledge on the accuracy of the phase angle correction.

5.4. Phobos

The irregular shape combined with the viewing geometry provide a challenge in determining the absolute brightness of Phobos at the time of our observations. It was decided not to attempt to constrain the absolute photometry but instead to focus on the relative photometry between the 4 filter bandpasses.

The key element in the calculation is the spectral reflectance over the wavelength range of the instrument. The spectral gradient is given by

$$S'(\lambda_1, \lambda_2, \lambda_{ref}) = \frac{1}{\rho_{ref}} \frac{\rho_{\lambda_2} - \rho_{\lambda_1}}{\lambda_2 - \lambda_1} \tag{3}$$

(Thomas, 2020) where ρ is the reflectivity at a wavelength, λ. A linear fit to the spectral reflectance of Phobos was made by Thomas et al. (1999) on the basis of Mars Pathfinder spectral imaging of the Mars-facing

hemisphere. This led to a spectral gradient of 7.9% (100 nm)$^{-1}$ referenced to 600 nm over the range 400–1000 nm. More recent observations by the OMEGA instrument on Mars Express (Bibring et al., 2004) show that a linear function for the spectral gradient over the full wavelength range of CaSSIS is an inadequate approximation.

Fig. 10 shows the results of an analysis of a series of spectral images of Phobos acquired by OMEGA. The signals from Phobos in OMEGA spectral images, ORB8974_0, ORB7915_3, ORB9574_0, ORB9586_0, ORBB085_0, and ORB5851_2 were extracted and summed to produce a final spectrum with higher signal-to-noise. The individual spectra were taken from a range of geometries and hence constitute an "average". The OMEGA data longward of 974 nm were not used because of the large inconsistencies between individual spectra. A linear fit was made to the data between 476 and 974 nm. This was extrapolated to longer wavelengths to cover the full wavelength range of CaSSIS. The slope of the fit was 8.2% (100 nm)$^{-1}$ and therefore very similar to the Mars Pathfinder result. The slopes for individual spectra range from $\approx$ 4% (100 nm)$^{-1}$ to over 11% (100 nm)$^{-1}$. The bluer part of Phobos is near Stickney and this crater is just beyond the limb in the CaSSIS images. It can be seen that the spectrum deviates significantly from a linear function below 450 nm and this must be accounted for in calibration of the BLU and, to a lesser extent, PAN filters.

It is trivial to scale the results to match the observations by modifying the albedo and the visible area but this provides no useful information for the task. In effect, we have a variable in eq.(1) instead of the detector gain. On the other hand, the relative responses between the filters should be indicative. As with Jupiter, the interest in checking against Phobos is that the illumination spectrum is roughly solar. Furthermore, the reflectance of Phobos is more similar to that of common Martian surfaces than the absorption line dominated spectrum of Jupiter. Hence, while there are huge uncertainties in the absolute photometry that can be addressed through study of other objects, the relative photometry is of interest.

6. Results and discussion

Table 3 shows the observed signal to predicted signal ratio for all objects considered here and for all filters. The values are expressed as a percentage. It can be seen immediately that only one value is close to 100% indicating that CaSSIS is, on average, less sensitive that predicted by use of eq. (1) with the best available transmissions, reflectances, and quantum efficiencies of the components at the nominal detector temperature. We illustrate this further by plotting these values in Fig. 11. There are many points to note.

1. The observations of HR4554 and HR5191 were acquired on the same day in the same observing run with the same sequence. Only the exposure times were modified slightly. They were calibrated in exactly the same way. However there is an $\approx$ 20% difference between the absolute photometric responses of the two stars. Note also that the trends from BLU to NIR of the two stars are almost identical. This suggests to us that the absolute photometry of one or both of the stars is not accurate. The ESO database indicates that the spectrophotometry for HR4554 is modelled and uncertain. It is recommended not to use this star for absolute flux calibration. The results here would suggest that this is indeed not advisable as HR5191 is consistent with the other observations while HR4554 is definitely not. HR5191 is also indicated as being unreliable and has therefore also been excluded although we note that including it has no influence on the results within error.

2. The mean of the observations of Jupiter, HR718, and HR1544 have been used to determine an absolute difference between the observed and expected values (Fig. 11). This is shown by the dashed line with an associated standard deviation for each filter. The standard deviation on the RED filter observations between the 3 targets is <1%. The
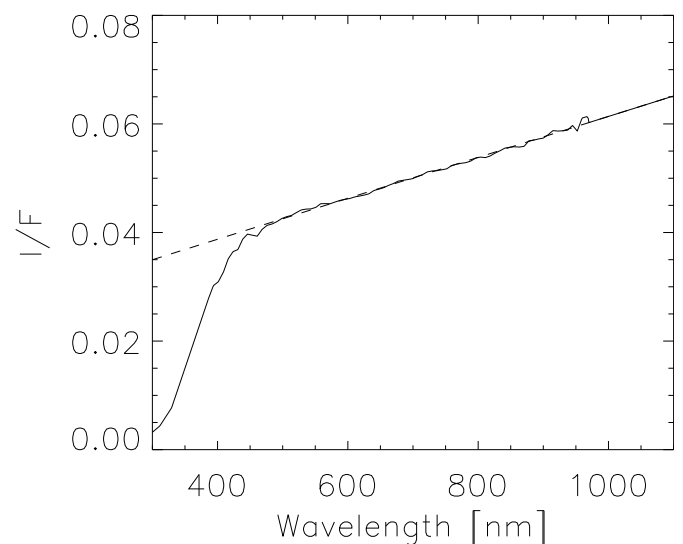

Fig. 10. Solid line: Mean reflectance of Phobos from 6 OMEGA cubes (ORB8974_0, ORB7915_3, ORB9574_0, ORB9586_0, ORBB085_0, and ORB5851_2). Because of the different geometries, the y axis has no real physical meaning and should be thought of as a relative reflectance. Dashed line: A linear fit to the data between 476 and 974 nm to derive a spectral gradient for comparison with other observations. Note, in particular, the drop in relative reflectance in the blue with respect to this spectral gradient.
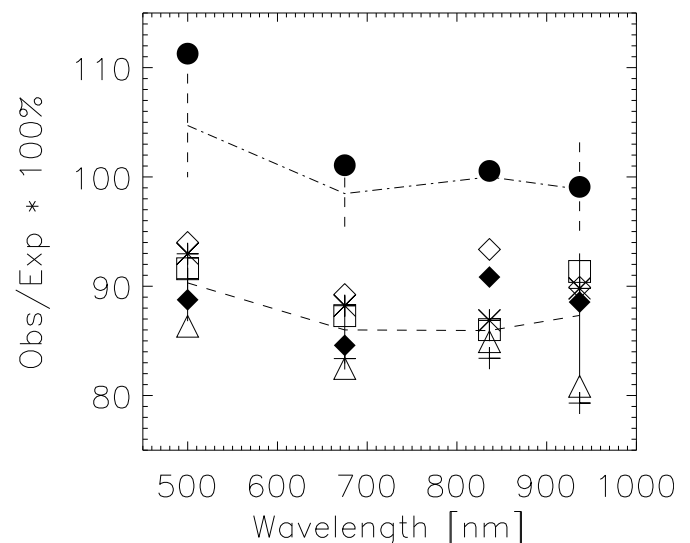

Fig. 11. The ratios of observed signal to that expected for the 7 observations for which we have high quality data assuming a quantum efficiency appropriate for 273 K. Open diamond: Phobos lower phase angle. Filled diamond: Phobos higher phase angle. Triangle: Jupiter. Square: HR718. Asterisk: HR1544. Filled circle: HR4554. Plus: HR5191. The dashed line provides the mean of the 3 observations for which absolute photometry can be defined (i.e. excluding Phobos, HR4554, and HR5191). A standard deviation for the 3 measurements is given by the vertical solid lines. The dot-dash line is the relative mean including Phobos, HR4554, and HR5191 and normalised to 100% for the red filter. This shows the relative colour dependence.

standard deviation is around 3% for PAN and BLU and around 5% for NIR which is much larger than the standard deviation in the digital number generation rate (of the order of 1–2% see Table 2) and hence the uncertainty is dominated by the uncertainty in the absolute fluxes from the respective targets and/or the system model. On average, over all filters, CaSSIS has a sensitivity of 86.9% of that expected from a calculation using data for the individual elements of the system.

This difference is quite large for such a simple system and hence it is interesting to discuss its possible origin.

Errors in the filter measurements at this level are highly improbable. The telescope mirror coating reflectance appears to the 4th power in the system model (there are four mirrors) but even here a 2–3% error in the reflectance measurement would normally be considered large with commercial portable reflectometers easily reaching this level. Although the specific QE of the detector may not be entirely accurate, a >10% error over the full wavelength range is implausible. Contamination and/or scattering may play a role but this is again rather a large amount of loss without any noticeable effect on image quality. The primary mirror is oversized and hence edge effects play no role. Manufacturing errors would normally lead to scattered light and there is little evidence of this for the stellar targets although the optical design, with the intermediate field stop between M2 and M3, should be rather efficient at eliminating scatter from the primary. In conclusion, there is no immediately obvious cause of the discrepancy but a re-evaluation of the mirror coating reflectance may be warranted.

3. The relative reflectance has been computed by normalizing to the RED filter and averaging over all targets (this time including both Phobos observations and the two stars, HR4554 and HR5191). It is clearly seen here that the relative responses of PAN, RED and NIR are well predicted by the model with detector temperature set to 273 K. The differences between them in this model are <1.5%. Changing the temperature of the detector modifies the QE significantly in the near-IR as shown in Fig. 9. A recalculation of the predicted signals using 294 K produces a change between RED and NIR relative response of −3.9%. This is comparable to the standard deviation of the measurements (4.3%). This indicates that indeed the temperature dependent QE of the detector should be accounted for but that differences between room temperature and 273 K are only significant at the 1σ level.

The BLU and the PAN filters show higher (+4.7%) and lower (−1.5%) sensitivity with respect to RED, respectively. The temperature dependence of the QE in the blue part of the spectrum does not provide an adequate explanation. To match the response in these two filters would require temperatures far below those used in the instrument and would also lead to poor agreement in the near-IR. From a pure statistical viewpoint, the relative differences are comparable to (BLU) or less than (PAN, NIR) the 1σ uncertainty but there is a common trend in the results for the different objects suggesting that the uncertainties may be overestimated. There is no obvious explanation for this inconsistency although inaccuracy in the QE in the blue part of the spectrum (where there is steep increase with wavelength) may play a role.

If we now assume that the sensitivity of CaSSIS is indeed only 86.9% of the expected value and that there are small correction factors needed for BLU, PAN and NIR to correct the relative responses with respect to RED, we can compute the conversion factors needed to go from the digital number generation rate in [DN s^{-1}] to I/F by rearranging eq. (1), setting the flux to that of a perfectly diffusing surface at 1 AU, and including the solid angle of the instrument, viz.

$$R_s = k \frac{1}{G} \int_0^\infty F_\odot(\lambda) \, M(\lambda) \, Q(\lambda) \, T(\lambda) \frac{\pi d^2}{4} \frac{\lambda}{hc} \frac{\Omega}{\pi} \, d\lambda \quad (4)$$

where Ω is the solid angle of a CaSSIS pixel (equal to 1.29 10^{-10} sr) and k is the correction factor needed to be applied based on our calibration. Table 4 provides the results. The table shows the original calibration factors, the correction factor needed and the recommended calibration factors based on this analysis. The values should be understood as follows. The I/F in the image is obtained by multiplying the observed digital number by the square of the heliocentric distance (r_h), dividing by the exposure time and then multiplying by the calibrated response value for

Table 4

Predicted and calibrated response values for converting the output digital numbers in CaSSIS images (after bias and flat-field correction) into I/F. Correction factor is the change in the absolute calibration compared to version 1 of the publicly released CaSSIS data in the Planetary Science Archive. I/F to rad. provides a further conversion factor which allows one to go back from I/F to radiance (in units of [W m^{-2} sr^{-1} nm^{-1}]) if the target is 1 AU from the Sun. I/F divided by this factor gives the radiance. The calculated error on the calibrated responses is estimated to be 2.8% with the assumed errors on the fluxes from the standard targets being dominant.

Filter	BLU	PAN	RED	NIR
Predicted response [reflectance/(DN s^{-1})]x 10^{-8}	2.613	1.307	3.472	3.589
Calibrated response [reflectance/(DN s^{-1})]x 10^{-8}	2.793	1.481	3.857	3.975
Correction factor	0.949	0.903	0.915	0.904
I/F to rad.	1.69	2.34	3.32	4.09

the appropriate filter (R_s). The correction factor indicates the difference to the existing calibration as used to produce version 1 of the CaSSIS data set in the Planetary Science Archive of ESA. (Note the conversion factor from DN to I/F used is given in the XML headers of version 1 of the archived CaSSIS data. The correction factor is not equal to the ratio of the predicted to calibrated response because, in the predicted response shown here, we have taken into account improved values for the QE and the new solar flux values of Meftah et al. (2018). These updates occurred after the delivery of version 1 to the PSA.)

7. Summary of uncertainties

In Table 5, we summarize the uncertainties to estimate the final uncertainty in the I/F values. The table shows that the measurement error from CaSSIS is smaller than the uncertainty in the fluxes from the targets. This should not be surprising for an instrument that, in principle, can reach a signal-to-noise ratio in excess of 100 for a single observation. The biggest question marks are in the accuracy in the knowledge of the fluxes and particularly the standard stars. The estimate for the standard stars here is based on an assessment by Megessier (1995). Using two stars and Jupiter the estimate in Table 5 would imply an error in the absolute calibration of 2.7% from this source alone (assuming one can add the uncertainties in quadrature). Incorporating all other errors (and again making the rather optimistic assumption that the errors can be added in quadrature), we obtain an error of 2.8%.

8. Conclusions

We have presented a calibration of the absolute response of the CaSSIS instrument onboard TGO based upon observations of standard stars and Jupiter and compared this to predictions based upon the optical design and the transmissions, reflectances, and responses of the various

Table 5

Uncertainties in the derived absolute calibration.

Item	Est. Uncertainty [%]	Comment
Bias	≤0.22	
Flatfield	0.072	
Residual background	0.2	
Star measurements	0.79	Assuming 10 obs. at 2.5% per obs.
Jupiter measurement	0.8%	Filter dependent. Value given for BLU.
Jupiter variability	3.7	
Star abs. fluxes	≈2.0	Vega is known to better than 0.7% but other standards are less well known

components. The photometric calibration has also taken into account the revised solar flux of Meftah et al. (2018). Observations of Phobos have also been used to give further confidence in the relative colour response although it is clear that Phobos is not a good standard because of the colour variability over its surface.

CaSSIS has 86.9% of the sensitivity of a model calculation based upon an analysis of the individual components (normalised to the RED filter). The uncertainties in the signal levels themselves, following detailed radiometric calibration, are no greater than 2.5% per image with this uncertainty reducing when more images are brought into the calculation. We estimate a final uncertainty of $\approx 2.8\%$ on the absolute calibration of the instrument with this uncertainty being dominated by the uncertainty in the knowledge of the standards being used. Further observations of standard stars and planetary targets are being made to provide additional confidence in these results and an update at the end of the mission is expected.

Small differences between observed relative signal levels in the filters when compared to the model suggest that additional corrections to the conversion factors required to convert observed digital number to reflectance should be made. Normalizing to the RED filter, the NIR and PAN filter observations are very close to the model with a correction factor of 1.1% and 1.5% relative to RED (and thus inside our uncertainties) respectively. For the BLU filter, the corrections are larger than the radiometric calibration uncertainty suggesting that use of this relative correction factor should improve the colour calibration between filters. The formal uncertainty however when computed over several different targets is around 4.3% in NIR, 3.3% in PAN and 4.7% in BLU. Hence, from a formal point of view, the model is consistent with the observation. The trend in the results is quite evident, however, but what is also noticeable is that the model predictions for solar-like targets (Jupiter and Phobos) are better than for the stellar targets. This might be a consequence of signal being missed in the extreme wings of the PSF in the case of point sources whereas the resolved sources are less sensitive to such errors.

The larger uncertainties found for the BLU filter observations are almost certainly a consequence of inadequate definition and/or inaccuracy of the quantum efficiency curve in the 380–430 nm range. The QE of the detector increases rapidly with wavelength in this range and uncertainty in the QE measurements can lead to significant changes in the predicted response. Further observations of stars of various spectral classes and planetary targets on a more regular basis should help to assess whether any further correction is needed. Despite the results indicating that the differences between filters are smaller than the uncertainty (at least for PAN and NIR relative to RED), we have incorporated the differences into our final calculations to produce absolute calibration factors for the four filters individually and these are presented in Table 4.

Data set availability

The data used for these analyses are archived in ESA's Planetary Science Archive (PSA). Data are released after a proprietary period of 6 months. The Jupiter, Phobos, and early standard star images are already available while the most recent observation from January 2021 should be available for download before the end of 2021.

Author statement

NT – performed the photometric analyses, reduced the solar system target observation and wrote most of the text.

AP – performed the radiometric calibration, extracted signals from stars, and wrote text.

MA – prepared the standard star acquisition sequences.

MR – supervised the telemetry conversion pipelines for the non-standard image acquisitions.

GC – criticised and corrected the manuscript.

ES – provided support and advice on the QE of the detector.

GM – criticised and corrected the manuscript.

TW – provided support and analyses on the optical performance of the telescope.

Declaration of competing interest

The authors declare that they have no known competing financial interests or personal relationships that could have appeared to influence the work reported in this paper.

References

Bibring, J.P., Soufflot, A., Berthé, M., Langevin, Y., Gondet, B., Drossart, P., Bouyé, M., Combes, M., Puget, P., Semery, A., Bellucci, G., Formisano, V., Moroz, V., Kottsov, V., Bonello, G., Erard, S., Forni, O., Gendrin, A., Manaud, N., Poulet, F., Poulleau, G., Encrenaz, T., Fouchet, T., Melchiori, R., Altieri, F., Ignatiev, N., Titov, D., Zasova, L., Coradini, A., Capacionni, F., Cerroni, P., Fonti, S., Mangold, N., Pinet, P., Schmitt, B., Sotin, C., Hauber, E., Hoffmann, H., Jaumann, R., Keller, U., Arvidson, R., Mustard, J., Forget, F., 2004. OMEGA: observatoire pour la Minéralogie, l'Eau, les Glaces et l'Activité. In: Wilson, A., Chicarro, A. (Eds.), Mars Express: the Scientific Payload, pp. 37–49 volume 1240 of ESA Special Publication.

Cremonese, G., Capaccioni, F., Capria, M.T., Doressoundiram, A., Palumbo, P., Vincendon, M., Massironi, M., Debei, S., Zusi, M., Altieri, F., Amoroso, M., Aroldi, G., Baroni, M., Barucci, A., Bellucci, G., Benkhoff, J., Besse, S., Bettanini, C., Blecka, M., Borrelli, D., Brucato, J.R., Carli, C., Carlier, V., Cerroni, P., Cicchetti, A., Colangeli, L., Dami, M., Da Deppo, V., Della Corte, V., De Sanctis, M.C., Erard, S., Esposito, F., Fantinel, D., Ferranti, L., Ferri, F., Ficai Veltroni, I., Filacchione, G., Flamini, E., Forlani, G., Fornasier, S., Forni, O., Fulchignoni, M., Galluzzi, V., Gwinner, K., Ip, W., Jorda, L., Langevin, Y., Lara, L., Leblanc, F., Leyrat, C., Li, Y., Marchi, S., Marinangeli, L., Marzari, F., MazzottaÂ Epifani, E., Mendillo, M., Mennella, V., Mugnuolo, R., Muinonen, K., Naletto, G., Noschese, R., Palomba, E., Paolinetti, R., Perna, D., Piccioni, G., Politi, R., Poulet, F., Ragazzoni, R., Re, C., Rossi, M., Rotundi, A., Salemi, G., Sgavetti, M., Simioni, E., Thomas, N., Tommasi, L., Turella, A., Van Hoolst, T., Wilson, L., Zambon, F., Aboudan, A., Barraud, O., Bott, N., Borin, P., Colombatti, G., ElÂ Yazidi, M., Ferrari, S., Flahaut, J., Giacomini, L., Guzzetta, L., Lucchetti, A., Martellato, E., Pajola, M., Slemer, A., Tognon, G., Turrini, D., 2020. SIMBIO-SYS: scientific cameras and spectrometer for the BepiColombo mission. Space Sci. Rev. 216, 75.

Danielson, G.E., Kupferman, P.N., Johnson, T.V., Soderblom, L.A., 1981. Radiometric performance of the Voyager cameras. J. Geophys. Res. 86, 8683–8689.

Gambicorti, L., Piazza, D., Pommerol, A., Roloff, V., Gerber, M., Ziethe, R., El-Maarry, M.R., Weigel, T., Johnson, M., Vernani, D., Pelo, E., Da Deppo, V., Cremonese, G., Ficai Veltroni, I., Thomas, N., 2017. First light of Cassis: the stereo surface imaging system onboard the exomars TGO. In: Society of Photo-Optical Instrumentation Engineers (SPIE) Conference Series, p. 105620A volume 10562 of Society of Photo-Optical Instrumentation Engineers (SPIE) Conference Series.

Gelino, C., Marley, M., 2000. Variability in an unresolved jupiter. In: Griffith, C.A., Marley, M.S. (Eds.), From Giant Planets to Cool Stars, p. 322 volume 212 of Astronomical Society of the Pacific Conference Series.

Hamuy, M., Suntzeff, N.B., Heathcote, S.R., Walker, A.R., Gigoux, P., Phillips, M.M., 1994. Southern spectrophotometric standards. II. Publ. Astron. Soc. Pac. 106, 566.

Hamuy, M., Walker, A.R., Suntzeff, N.B., Gigoux, P., Heathcote, S.R., Phillips, M.M., 1992. Southern Spectrophotometric Standards. I. Publ. Astron. Soc. Pac. 104, 533.

Karkoschka, E., 1998. Methane, ammonia, and temperature measurements of the jovian planets and Titan from CCD-spectrophotometry. Icarus 133, 134–146.

Kurucz, R.L., Furenlid, I., Brault, J., Testerman, L., 1984. Solar Flux Atlas from 296 to 1300 Nm.

Mayorga, L.C., Jackiewicz, J., Rages, K., West, R.A., Knowles, B., Lewis, N., Marley, M.S., 2016. Jupiter's phase variations from Cassini: a Testbed for future direct-imaging missions. Astron. J. 152, 209.

McEwen, A.S., Eliason, E.M., Bergstrom, J.W., Bridges, N.T., Hansen, C.J., Delamere, W.A., Grant, J.A., Gulick, V.C., Herkenhoff, K.E., Keszthelyi, L., Kirk, R.L., Mellon, M.T., Squyres, S.W., Thomas, N., Weitz, C.M., 2007. Mars Reconnaissance Orbiter's high resolution imaging science experiment (HiRISE). J. Geophys. Res. 112, E05S02.

Meftah, M., Damé, L., Bolsée, D., Hauchecorne, A., Pereira, N., Sluse, D., Cessateur, G., Irbah, A., Bureau, J., Weber, M., Bramstedt, K., Hilbig, T., Thiéblemont, R., Marchand, M., Lefèvre, F., Sarkissian, A., Bekki, S., 2018. SOLAR-ISS: a new reference spectrum based on SOLAR/SOLSPEC observations. Astron. Astrophys. 611, A1.

Megessier, C., 1995. Accuracy of the astrophysical absolute flux calibrations: visible and near-infrared. Astron. Astrophys. 296, 771.

Roloff, V., Pommerol, A., Gambicorti, L., Servonet, A., Thomas, N., Brändli, M., Casciello, A., Cremonese, G., Da Deppo, V., Erismann, M., Ficai Veltroni, I., Gerber, M., Gruber, M., Gubler, P., Hausner, T., Johnson, M., Lochmatter, P., Pelò, E., Sodor, B., Szalai, S., Troznai, G., Vernani, D., Weigel, T., Ziethe, R., Zimmermann, C., 2017. On-ground performance and calibration of the ExoMars Trace Gas Orbiter CaSSIS imager. Space Sci. Rev. 212, 1871–1896.

Simioni, E., De Sio, A., Da Deppo, V., Naletto, G., Cremonese, G., 2017. CMOS detectors: lessons learned during the STC stereo channel preflight calibration. In: Society of Photo-Optical Instrumentation Engineers (SPIE) Conference Series, p. 105622M

volume 10562 of *Society of Photo-Optical Instrumentation Engineers (SPIE) Conference Series*.

Simioni, E., Re, C., Mudric, T., Cremonese, G., Tulyakov, S., Petrella, A., Pommerol, A., Thomas, N., 2021. 3dpd: a photogrammetric pipeline for a push frame stereo cameras. Planet. Space Sci. 198, 105165.

Stetson, P.B., 1987. DAOPHOT: a computer program for Crowded-field stellar photometry. Publ. Astron. Soc. Pac. 99, 191.

Thomas, N., 2020. An Introduction to Comets - Post-Rosetta Perspectives. Springer.

Thomas, N., Britt, D.T., Herkenhoff, K.E., Murchie, S.L., Semenov, B., Keller, H.U., Smith, P.H., 1999. Observations of Phobos, Deimos, and bright stars with the imager for Mars pathfinder. J. Geophys. Res. 104, 9055–9068.

Thomas, N., Cremonese, G., Ziethe, R., Gerber, M., Brändli, M., Bruno, G., Erismann, M., Gambicorti, L., Gerber, T., Ghose, K., Gruber, M., Gubler, P., Mischler, H., Jost, J., Piazza, D., Pommerol, A., Rieder, M., Roloff, V., Servonet, A., Trottmann, W., Uthaicharoenpong, T., Zimmermann, C., Vernani, D., Johnson, M., Pelò, E., Weigel, T., Viertl, J., De Roux, N., Lochmatter, P., Sutter, G., Casciello, A., Hausner, T., Ficai Veltroni, I., Da Deppo, V., Orleanski, P., Nowosielski, W., Zawistowski, T., Szalai, S., Sodor, B., Tulyakov, S., Troznai, G., Banaskiewicz, M., Bridges, J.C., Byrne, S., Debei, S., El-Maarry, M.R., Hauber, E., Hansen, C.J., Ivanov, A., Keszthelyi, L., Kirk, R., Kuzmin, R., Mangold, N., Marinangeli, L., Markiewicz, W.J., Massironi, M., McEwen, A.S., Okubo, C., Tornabene, L.L., Wajer, P., Wray, J.J., 2017. The colour and stereo surface imaging system (CaSSIS) for the ExoMars Trace Gas Orbiter. Space Sci. Rev. 212, 1897–1944.

Thomas, N., Keller, H.U., 1990. Photometric calibration of the Halley Multicolour Camera. Appl. Opt. 29, 1503–1519.

Tomasko, M.G., 1976. Photometry and polarimetry of Jupiter. In: Jupiter. Univ. Arizona Press, pp. 486–515.